Publications of the Astronomical Society of the Pacific, 132:033001 (16pp), 2020 March https://doi.org/10.1088/1538-3873/ab6818

Estimating Electron Temperatures in Ionized Nebulae: The Direct Method and its Limitations

David C. Nicholls[1,2], Lisa J. Kewley[1,2], and Ralph S. Sutherland[1,2]
[1] Research School of Astronomy and Astrophysics, Australian National University, Canberra, ACT, Australia; david.nicholls@anu.edu.au
[2] ARC Centre of Excellence for All Sky Astrophysics in 3 Dimensions (ASTRO 3D), Australia
Received 2019 November 12; accepted 2020 January 6; published 2020 January 28

Abstract

In this paper we examine the Direct Method for measuring electron temperatures in H II regions, and the extent to which such measurements can provide meaningful information on the physical conditions in these regions. We discuss the limits to what can be inferred about electron temperatures from nebular emission line fluxes. We provide a new simplified method for estimating electron temperatures, including parameters that can be used to determine this from UV [O III] and [O II] oxygen lines observable in high-redshift objects using ground-based telescopes. We test this method on published UV high redshift observations and compare the results with reported electron temperatures.

Key words: HII regions – ISM: abundances

Online material: color figures

1. Introduction

Emission lines from an H II region contain information on the physical conditions in the nebula and the nature of the star formation processes, leading to a better understanding of stellar properties and the chemical evolution of the universe. The forbidden lines of O^{++} (*inter alia*) provide information on the electron temperature (T_e), while other emission lines can provide information on electron densities, typically from the ratio of the 6716, 31 Å lines of S^{+}. These and other lines can inform us about the ionization conditions and and chemical abundances in a nebula.

However, all such observations are of the emission line fluxes integrated through the whole emission region. As these fluxes are nonlinear functions of temperature, pressure, ionization parameter, density, and metallicity, inverting the observed fluxes to obtain profiles for these parameters is not possible.

A nebula may be approximately at a constant pressure if the sound crossing time is less than the age of the ionized region, but the electron temperature and density are unlikely to be constant. We can only hope to measure average values for temperature and density.

So what can we know about temperatures, densities, etc. from our observations? In this paper we explore that question, to identify the circumstances under which the measured quantities may provide a useful indication of physical parameter values.

We describe the Direct Method, using the forbidden lines of O^{++}, and its physical basis. Then we examine how the results of this method relate to the actual physical parameters the method aims to measure. This leads us to identify the conditions under which the measurements can provide reasonably accurate and useful results. We argue that given the uncertainty about the structure of a nebula, simple methods for determining the electron temperature are as useful as the more complex ones, and we provide a series of new simple algebraic fits to generate values for the electron temperature, for both the usual optical emission lines of oxygen and related UV lines. These will be increasingly useful in high redshift observations. We compare the results of this method with those from published observations. Finally, we provide a method for using the optical and UV [O II] lines as a temperature diagnostic with the virtue that the density and temperature diagnostic emission lines arise from the same nebular regions.

2. Background

When the identity of the prominent 4959 Å and 5007 Å lines in the spectra of H II regions had been identified as arising from collisionally excited forbidden lines of [O III], over 90 yr ago (Bowen 1928), it was realized that the ratio of the fluxes of these lines to the fainter 4363 Å line could provide a measure of the relative populations in the $^1D_2$ and $^1S_0$ levels of the O^{++} ion (Hebb & Menzel 1940), and thus of the temperature of the electron population responsible for exciting these ions. This fact has been widely used since then to measure the electron temperature in nebulae.

Many methods to measure nebular electron temperatures have been proposed (see Stasińska 2004), most using the

measured fluxes of either collisionally excited emission lines or recombination lines. Here we focus on the collisionally excited emission lies, and in particular the optical and UV oxygen lines.

As the fluxes of collisionally excited emission lines are a direct measure of the populations of the originating energy levels, and thus of the electron temperature, this technique is known as the "Direct Method," to distinguish it from secondary, calibrated methods using strong emission lines.[3] Using the bright forbidden lines of [O III], this method was expressed in its current form by (Seaton 1975, Equations 2.2 and 2.3) and updated by Aller (1984), Osterbrock (1989) and Osterbrock & Ferland (2006).

Several ion species have been used to measure electron temperatures, including O, O^+, O^{++}, Ne^{++}, S^+, S^{++}, and N^+ (see for example Osterbrock & Ferland 2006). The main requirements are that the emission lines from the excited states be readily observable in nebular spectra, and that the electron density be below the critical density for the ion. For this reason, the most widely used are the forbidden collisionally excited lines of [O III] at 4363 and 5007, 4959 Å. If high redshift spectra are available, or in space-based observations, UV [O III] lines can also be used to estimate electron temperatures. For the O^{++} ion, these calculations depend on the relative populations in the $^1D_2$, $^1S_0$ and $^5S_2$ levels.

Several implementations of the Direct Method are available to the observer, with varying levels of complexity, for example, the formula presented in Osterbrock & Ferland (2006) (Equation 5.4) and the related iterative method described by Izotov et al. (2006), IRAF STSDAS NEBULA TEMDEN (http://stsdas.stsci.edu/nebular/), the Nebular Empirical Analysis Tool (Wesson et al. 2012), and the PyNeb application (Luridiana et al. 2012). Each depends on the accuracy and completeness of the atomic data. Older methods may use old atomic data which will yield less reliable results. There is still some uncertainty in the computed collision strengths for O^{++} (Storey et al. 2014). However, this does not have a major effect on the results obtained from observed fluxes in the presence of observational measurement uncertainties. Finally, it is important to note that a key feature of the Direct Method is that it is based on the line flux ratio from atoms at a single temperature and density. This is seldom the case in real H II regions and leads to the problems we will address below.

3. The Atomic Basis of the "Direct Method"

Figure 1 shows the energy levels of O^{++} and the transitions giving rise to the major collisionally excited emission lines in the visible and UV that can be used to estimate the local electron temperature. This approach depends on the collisional excitation of ions by electrons to (and de-excitation from) energy levels ($^1D_2$, $^1S_0$ and $^5S_2$) above the ground state. The higher the electron temperature, the greater the populations in the higher levels. The higher the density, the greater the collisional de-excitation. If we know the collisional strengths and the transition probabilities, using observed emission line fluxes, we can derive an estimate of the temperature of the electrons responsible for exciting the ions.

Following Osterbrock (1989) and Osterbrock & Ferland (2006), in the low density limit (typically $n_e < 100\,\mathrm{cm}^{-3}$ for O^{++}), we can express the flux ratio of the 4959 + 5007 and 4363 Å lines as:

$$\frac{j_{\lambda4959} + j_{\lambda5007}}{j_{\lambda4363}} = \left[\frac{\Upsilon_{^3P,^1D}}{\Upsilon_{^3P,^1S}}\right] \times \left[\frac{A_{^1D_2,^3P_2}\,\nu(\lambda5007) + A_{^1D_2,^3P_1}\,\nu(\lambda4959)}{(A_{^1D_2,^3P_2} + A_{^1D_2,^3P_1})\,\nu(\lambda4363)}\right] \times \left[\frac{A_{^1S,^1D} + A_{^1S,^3P}}{A_{^1S,^1D}}\right] \exp\left[\frac{E_{^1S,^1D}}{k\,T_e}\right], \quad (1)$$

where the flux at wavelength *xxxx*Å is $j_{\lambda xxxx}$, $\Upsilon(i, j)$ is the thermally averaged collision strength for collisional excitation between levels i and j, $A_{i,j}$ is the transition probability between levels i and j, $\nu(\lambda nnnn)$ is the wave number at wavelength nnnn Å, $E_{i,j}$ is the energy gap between levels i and j, k is the Boltzmann constant and T_e is the electron temperature.

Equation (1) expresses the relationship between T_e and the emission line flux ratio. It applies to a single electron temperature and low density where collisional de-excitation can be ignored. Taking electron density dependence into account, Osterbrock & Ferland (2006), following Aller (1984), simplify Equation (1) to:

$$\frac{j_{\lambda4959} + j_{\lambda5007}}{j_{\lambda4363}} = \frac{7.90\exp(3.29 \times 10^4/T_e)}{1 + 4.5 \times 10^{-4}(n_e/T_e^{1/2})} \quad (2)$$

Determining T_e from this equation defines the Direct Method. In addition to the emission line fluxes, a correction is necessary due to the density dependence of the line ratio. Standard implementations therefore involve estimating the electron density in order to calculate the electron temperature.

Equation (1) shows the dependence of the line flux ratios on collision strengths (Υ). For O^{++}, there are three sets of non-temperature-averaged collision strengths available, from Lennon & Burke (1994), Palay et al. (2012) and Storey et al. (2014).[4] We consider the collision strength data from Lennon & Burke (1994) to be the best choice for these calculations: their values are similar to the more recent work by Storey et al. (2014), but, unlike the latter, they include data from the 6th level ($^5S_2$). There is some uncertainty with the data from the

[3] Although see Kewley et al. (2019b) for new methods of estimating physical parameters directly from the main UV, optical and IR nebular emission lines.

[4] Other collision strength sets are available, but these are the only ones for which non-thermally averaged data are available, making them useful for non-Maxwellian energy distributions.

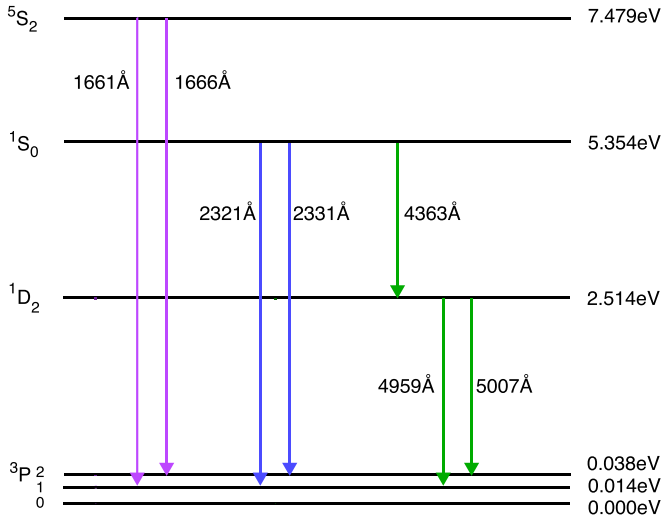

Figure 1. Lowest 6 energy levels of O^{++}. Transitions to the lowest of the triplet-P ground states are doubly forbidden and are usually faint.
(A color version of this figure is available in the online journal.)

alternative 6-level collision strength set from Palay et al. (2012), as discussed in Storey et al. (2014). In any case, the uncertainties in real observations are likely to far exceed the differences between the fits using different collision strengths. The computed diagnostic line flux ratios as functions of temperature and density for the O^{++} collision strengths from Lennon & Burke (1994) are given in Table 9 in the Appendix.

However, there are a number of problems with using this approach to measure temperatures, and these should be understood before simply reporting electron temperatures from observations.[5]

4. Discussion

4.1. Physical Characteristics of H_{II} Regions

We can make some general statements about H II regions.

1. Except in special cases, and then only approximately, H II regions are not uniform in temperature or density, so a single value for electron "temperature" or "density" is not necessarily an accurate estimate of the range of temperatures or densities in a nebula.
2. The observed [O III] emission line spectrum from an H II region is integrated through the nebula (or over the entire nebula when it is not spatially resolved) and the observed fluxes of [O III] may be dominated by the hottest and/or highest density zones.
3. H II regions are likely to be approximately uniform in pressure (after $\sim 10^5$ yr, when the expansion rate of the nebula becomes sub-sonic), when the sound crossing time is less than the age of the nebula.
4. As a consequence of the changing radiation field, temperature and density, fluxes from ions with different excitation energies and energy levels (e.g., O^{++} and S^{+}) peak in different zones in the nebula.
5. The hardness of the ionizing spectrum increases with distance from the ionizing source, with consequent changes in its heating effect.
6. The structure of an H II region is usually complex, so models which are spherical or planar are at best only approximations.
7. Strongly excited H II regions may exhibit shock wave spectra, which differ considerably from standard photo-ionized spectra. The presence of strong emission lines of [O I] and [S II] and emission lines of high ionization species of Fe may indicate the presence of shock waves, and/or supernova remnants (see e.g., Dopita et al. 2018).
8. It has been assumed for decades (e.g., Bohm & Aller 1947) that the electrons in H II regions are in Maxwell–Boltzmann (MB) equilibrium. However, while any particular location in an H II region is likely to be in local thermal equilibrium, that equilibrium may not be Maxwellian (e.g., Nicholls et al. 2012; Livadiotis 2018) . The equilibrium conditions are likely to differ throughout the nebula. In the absence of better information, however, it is conventional to assume MB equilibrium.

Given these complexities, we need to ask what are we actually measuring from the line flux ratios? It is important to understand the limitations of the Direct Method. It is not a matter of applying simple formulae automatically and expecting the "temperature" thus generated to be the final word on conditions in the nebula. In the following sections, we explore the circumstances under which the estimate may be expected to yield a physically realistic result.

4.2. The physical meaning of T_e

A single atom model doth not a nebula make (if it were so, we would not need Cloudy, Mappings and similar modeling codes.)

Electron temperatures derived from observed nebular emission line fluxes (Equations (1) and (2)), *do not necessarily* measure the physical electron temperatures in an ionized nebula. The electron temperature and oxygen line fluxes in such an environment vary throughout the ionized region. Observed line fluxes are the luminosity weighted average of conditions in the nebula. Direct Method formulae give the electron temperature of dust free, isolated oxygen atoms at a uniform electron density and a single electron temperature, with uniform photoionization, that generate the same emission line fluxes as the observed data. These *atomic equivalent temperatures* may be used to estimate an average temperature

[5] Note the admonition from Dr Strange, from the eponymous film, Marvel Films, 2016, "They really should put the warnings before this stuff."

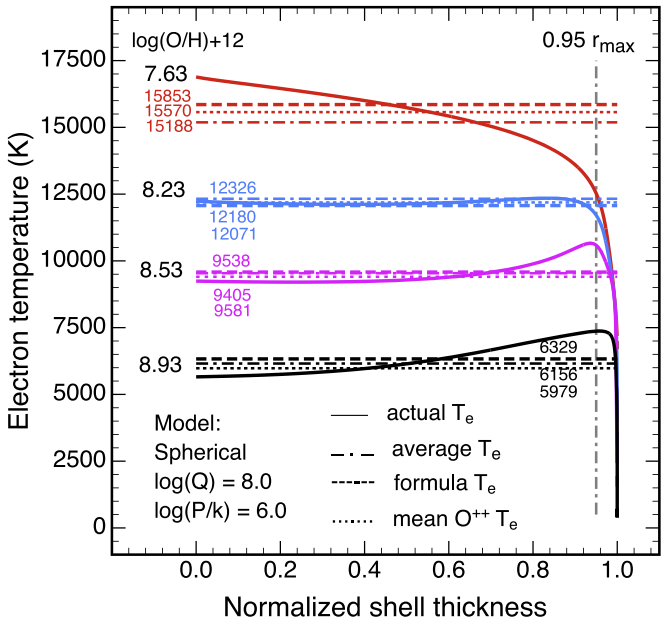

Figure 2. Electron temperatures (solid lines) through a model spherical (Strömgren Sphere) H II region. The atomic equivalent temperatures calculated from total [O III] line fluxes using Equation (2) are shown as dashed lines. The average electron temperatures through the nebula are marked as dashed–dotted lines. The average electron temperature encountered by the emitting O^{++} ions are shown as dotted lines.

(A color version of this figure is available in the online journal.)

and oxygen abundance, but do not take into account the heterogeneous structure of emission nebulae and the spatial variation of the photoionizing spectrum.

Under some circumstances, T_e calculated from single atom models can give a reasonable estimate of actual conditions. Figure 2 illustrates the intrinsic variation of electron temperatures for a spherical (Strömgren Sphere) model H II region with $\log(Q) = 8.0$ and $\log(P/k) = 6.0$, for metallicities between log (O/H)+12 = 7.63 and 8.93.[6] The dashed lines and associated numbers show the atomic equivalent (Direct Method) temperatures for each model, calculated from the total (observed) line fluxes. The average electron temperature encountered by the emitting O^{++} ions is shown as a dotted line. The difference between the dashed and dotted lines is explained by a small difference in the spatial distribution of the ions at different energy levels. In practice, the 4363 Å and other higher excitation [O III] lines are only observed from the hotter zones in a nebula and can provide only limited information about the cooler regions.

Table 1 shows three electron "temperatures" for each of the models in Figure 2. The Average T_e is the volume weighted temperature over the entire emitting region. It is the true average electron temperature of the model H II region. The Ionic T_e is the mean electron temperature experienced by the O^{++} ions over the part of the H II region where they generate the emission lines. The Formula T_e is the electron temperature calculated using the Direct Method. The values and their differences are only correct for this simple model, but illustrate the effects likely to be encountered in real nebulae. δT_e is the difference in electron temperatures between the inner shell radius and 0.95 of the 99% neutral maximum radius (marked as a vertical dashed–dotted line in Figure 2) and is a measure of the extent to which conditions deviate from isothermal.

Table 1
Electron Temperatures and O^{++} Metallicity Errors for the Models in Figure 2

Metallicity	Average *Te*	O++ ionic *Te*	Formula *Te*	δTe ($R_{0-0.95}$)	$\delta z(O^{++})$
7.63	15188	15570	15853	4353	0.02
8.23	12326	12189	12071	544	−0.04
8.53	9538	9405	9581	−1339	0.00
8.93	6156	5979	6329	−1714	n/a

Two features are apparent from Figure 2. At high metallicities, there can be substantial temperature gradients. As these high-gradient nebulae are are usually cool, the auroral emission lines from the upper energy levels are very faint compared to the 4959 and 5007 Å lines and difficult to observe. At very low metallicities, there may be similar temperature gradients, so the estimated electron temperature will only be a luminosity-weighted average. The electron temperatures calculated using standard methods fit the actual data well for intermediate values of metallicity, but less well for low or high metallicity. While real H II regions are seldom as simple as the models used here,[7] this result does give one confidence that the electron temperature computed from the line flux ratios can give a plausible measure of the physical conditions in the nebular region at intermediate metallicities.

Table 1 shows the data from Figure 2, the range of variation in actual T_e across the emission region (δTe ($R_{0-0.95}$)) and the error in the gas-phase metallicity for the O^{++} ion compared to model values ($\delta z(O^{++})$). The gas-phase metallicities for the O^{++} ion were calculated using Equation (5) from Izotov et al. (2006). The metallicity results for the [O III] emission region are very good. The "n/a" value is due to low [O III] 4363 Å flux at high metallicity (see Section 4.4.1).

[6] Where P is the pressure of the interstellar medium (ISM), k is the Boltzmann constant, and Q is the ionization parameter.

[7] Except where noted, the models presented in this paper were calculated in Mappings *V* (Sutherland 2019), using a composite stellar population from Starburst99 (Leitherer et al. 2014) with continuous star formation at 4 Myr, Salpeter IMF, using the WMBasic stellar atmospheres and Geneva 40% rotation evolutionary tracks. Specific input parameters such as pressure and ionization parameter are indicated in the figures and tables.

4.3. The Caveats

This leads us to a list of caveats that are intrinsic to measuring electron temperatures and other nebular parameters.

4.3.1. Single Atom Models

The Direct Method is based on comparing observations with calculations of emission fluxes from atoms at a single temperature and density. We know this is not an accurate picture of any H II region or other nebula. It is, as noted above, an *atomic equivalent temperature*. There is no single electron temperature in any nebula.

4.3.2. Co-spatiality with Density Measurements

Typically in observed H II regions, the sound crossing time is shorter than the age of the nebula. After an initial short period of supersonic expansion ($\sim 10^5$ yr), the expansion rate of the nebula slows to sub-sonic and the pressure has time to equilibrate (Kaplan 1966; Spitzer 1968). If the pressure is uniform (isobaric), given the changing radiation field throughout the nebula, the density (and temperature) will be non-uniform. Measuring a density in one region does not necessarily tell us about the density in another. Using the [S II] emission lines at 6716 and 6731 Å or the [O II] emission lines at 3726 and 3729 Å to estimate the electron density may be inappropriate for comparing with [O III] electron temperatures, as the regions where they are emitted are not co-spatial with the region from which the [O III] emissions arise.

4.3.3. Non-isothermal Nebular Structures

The models illustrated here demonstrate that even an H II region with simple geometry is not isothermal. Consequently, any "temperature" measured from emission line fluxes must be some form of average. As illustrated in Figure 2, there is a physically real average temperature for the whole emission region, and an average temperature for the region over which the relevant ionic species emits. The latter are only approximately estimated by the Direct Method and the former are not able to be measured (except approximately, using direct method techniques with other ions with different ionization energies).

Where other temperature diagnostic species with different excitation energies have observable emission lines, such as [S III], these can be used to estimate electron temperatures in different parts of a nebula (e.g., Binette et al. 2012). However, for most objects, the oxygen lines are likely to be the most readily measurable.

4.3.4. Luminosity Bias

Total fluxes observed from a distant H II region are dominated by the brightest regions of the nebula. Consequently, any attempt to derive an electron temperature by the Direct Method will give a result dominated by the conditions in the brightest zones. As these are likely to be the hotter regions, this will overestimate the average temperature and underestimate the metallicity. High density regions can also generate a luminosity bias.

4.3.5. Temperature or Density Diagnostic?

In order for an emission line flux ratio to function as a purely temperature diagnostic, the electron density, n_e, must be well below the lower of the critical densities of the two levels. The critical density is defined as that (temperature-dependent) density at which the rate of radiative de-excitation from the upper level of an atomic transition, equals the rate of collisional de-excitation. Below the critical density, the radiative flux increases with n_e^2 but above the critical density, the flux increases with n_e.

Critical density for collisional de-excitation is $7.0 \times 10^5\,\mathrm{cm}^{-3}$ for [O III] 5007 Å and $3.3 \times 10^7\,\mathrm{cm}^{-3}$ for [O III] 4363 Å. So while at low densities, the 4363/5007 flux ratio is a temperature diagnostic, it is also a density diagnostic, when the density is not much above or below the two critical densities (Baskin & Laor 2005). Densities of this order are normally only observed in planetary nebulae.

4.3.6. High Pressure Effects

As pressure increases the 5007 Å line will be quenched more rapidly than the 4363 Å line. Thus the 4363/5007 flux ratio will increase as pressure increases, and emulate a higher temperature (for example, in AGN, Nagao et al. 2001). This is especially important when we observe high luminosity, unresolved H II regions at high redshift. Observations of objects that are not spatially resolved in distant galaxies may give rise to higher apparent electron temperatures than are actually present. Under suitable conditions of pressure and temperature, a higher apparent electron temperature derived using the 1666 Å line, compared to that derived using the 4363 (or 2321)Å line may indicate a pressure bias is operating.

4.4. Complex Giant H_{II} Regions

The Tarantula Nebula (30 Doradûs) in the Large Magellanic Cloud is an analogous object to bright H II regions likely to be observed at high redshift. It has over 800 observed O-, WN- and luminous B-stars giving rise to the nebular excitation (Evans et al. 2011, and subsequent papers). Such an object is complex to model, especially when observed spatially unresolved at high redshift.

4.4.1. Fadeout

There is also a lower practical temperature limit for the Direct Method. The expression for the emissivity of a line includes the $\exp(-\Delta E/kT)$ term. Among the [O III] lines, ΔE for the 4363 Å line is greater than for the 4959 and 5007 Å lines, so the emissivity of the 4363 Å line decreases faster that for the 4959/5007 Å lines as

T_e falls. At some point, for any given observational signal-to-noise ratio (S/N) limit, the 4363 Å (and similar lines arising from the $^1S_0$ and $^5S_2$ levels) are no longer measurable, even though the 4959, 5007 Å lines are still observed. And at high metallicities (>1.0 solar), the emission lines of [O III] are for practical purposes, unobserved. These factors set limits for electron temperatures derived from the [O III] lines.

Finally, as the hot stars embedded in a nebula age, the excitation energy available to generate emission lines falls, and the fluxes of the diagnostic lines decreases to below observability. This is due both to the ability of the ionizing radiation to generate ions such as O^{++}, and to excite the diagnostic lines, even though the hydrogen recombination lines may still be strong.

5. Electron Density Considerations

Current methods for estimating electron temperatures (PyNeb, and the Aller/Osterbrock/Izotov equations) require a value for the electron density, to correct for the slight density dependence in the temperature diagnostic lines. The density, of course, is a parameter of interest in its own right.

As with electron temperatures, the electron density line ratios are calculated by comparing observed line fluxes against those generated in a theoretical assembly of atoms at a constant temperature and density, and are thus *atomic equivalent densities*, although the actual density, like the temperature, varies considerably throughout the emission region. The full radiative transfer models we use here are isobaric (constant pressure), so the temperature and density are conjugate variables. As noted earlier, this is a reasonable assumption when the sound-crossing time is less than the age of the nebula, allowing pressure equalization. Real H II regions are unlikely to be isochoric (constant density), except in the initial stages of the formation ($\sim 10^5$ yr) when the expansion rate is supersonic (Kaplan 1966; Spitzer 1968), a condition unlikely to be observed.

The most observationally convenient and often used method to measure electron densities (see Osterbrock & Ferland 2006) uses the ratio of the observed fluxes of the 6716 and 6731 Å [S II] emission lines, and the electron temperature. However, there are at least four possible values for n_e: the density calculated from the [S II] line flux ratio, the local density through the nebula, the average value of that quantity, and the average electron density experienced by the S^+ ions used to estimate n_e. These are illustrated in Figure 3, for a spherical nebular model calculated using Mappings *V*, with pressure log $(P/k) = 6.0$ and ionization parameter $\log(Q) = 8.0$, for four metallicities. Only the line flux ratio value is observable. The others must be estimated by matching nebular models to observed emission line fluxes from a range of ions.

Lack of co-spatiality is a particular concern: to allow for the variation of the [O III] temperature diagnostic with density, one needs to know the density before calculating the temperature. Likewise, it is necessary to know the temperature in order to calculate the density, due to the temperature dependence of the [S II] doublet flux ratio. In general no line ratio is purely a temperature diagnostic, or purely a density diagnostic. In practice, for normal H II regions, we assume that the sulphur doublet line ratio is density sensitive, and the [O III] line ratio is mainly temperature sensitive. Solving for both temperature and density simultaneously requires an iterative approach.

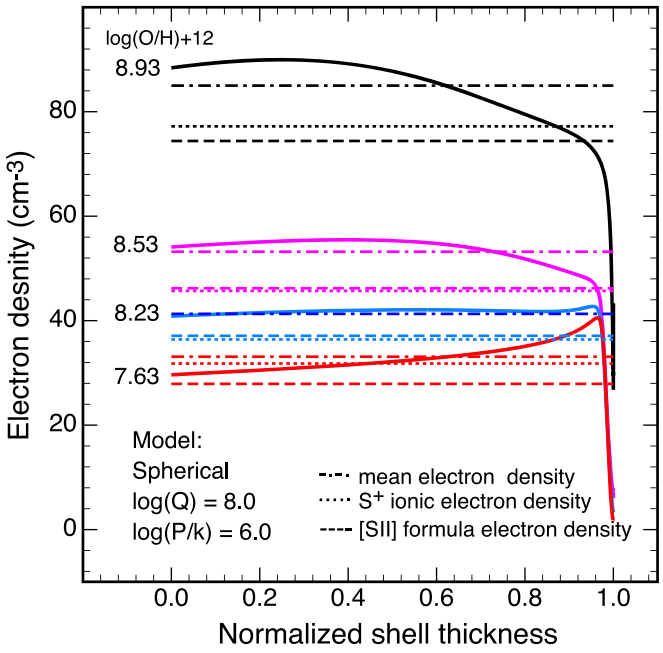

Figure 3. Electron densities. Solid lines: actual densities in the 300+ zones computed; dashed–dotted lines: nebular average of the actual densities; dotted lines: average of the electron densities experienced by the S^+ ions; dashed lines: values calculated using the [S II] line flux ratio and [O III] electron temperature, using PyNeb.
(A color version of this figure is available in the online journal.)

So when we use a value of electron density to compute the correction to the electron temperature, which value, if any, should be used? The value derived from the sulphur doublet flux ratio is the most often used method for measuring density, but from Figure 4, the [S II] emissions are obviously not co-spatial with the [O III] emissions. The use of precise formulae may give the observer a false sense of confidence that they are measuring conditions accurately. There are alternative density diagnostics, for example the flux ratio of the [O II] lines at 3726 and 3729 Å, and emission lines from [Cl III] and [Ar IV], which arise in different regions of a nebula. The [O II] line ratio requires observations with sufficient spectral resolution. Apart from the [O II] lines, most potential optical density diagnostic lines are faint.

Although new alternative density diagnostics have been proposed recently by Kewley et al. (2019a) that may have less co-spatial problems, we conclude that using the [S II] line flux ratio to correct for the density dependence of the [O III] lines may be a flawed approach in many cases, even though it is widely used and

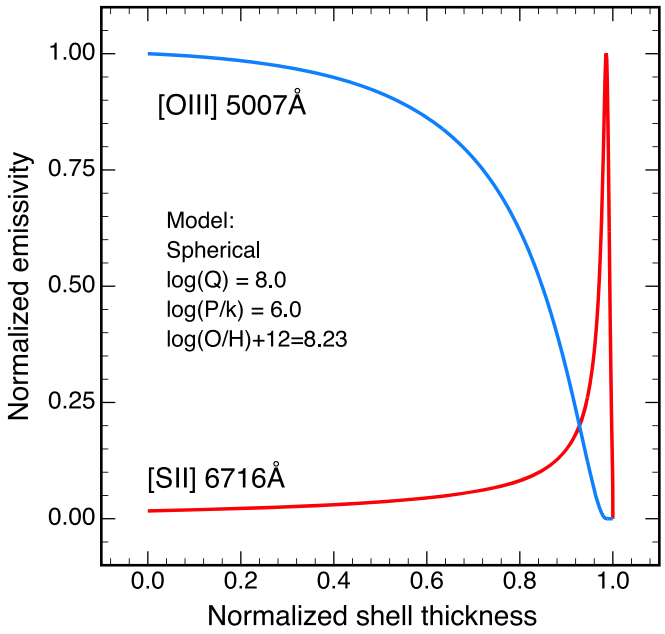

Figure 4. Lack of co-spatiality of the oxygen and sulphur lines in a spherical model nebula.
(A color version of this figure is available in the online journal.)

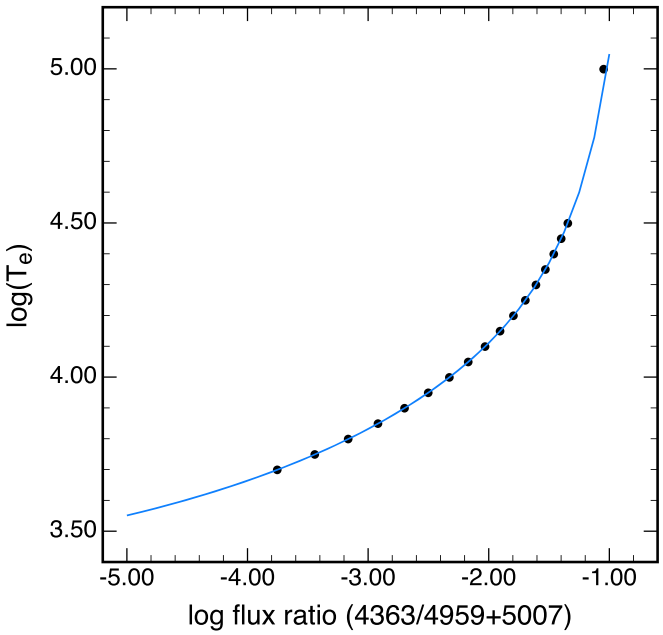

Figure 5. Illustrating the reliability of extrapolating rational polynomials: fit of rational quadratic polynomial (blue line) to Mappings *V* 5.1 computed data (dots) for the flux ratio using the O III lines at 4363, 4959 and 5007 Å. The fitted range is 5000–32,000 K. The outlier at 100,000 K (top right) was not used in the fit and indicates that the extrapolated fit curve behaves well at high temperatures outside the fit range. The rms error in log(T_e) for the fit range is 3.23E-05.
(A color version of this figure is available in the online journal.)

may be the only available method using observed emission lines. The question arises, is it worth making this correction at all?

6. A New Fitting Method

For electron densities in typical H II regions, as the electron temperature is a slowly varying function of electron density below $1000\,\mathrm{cm}^{-3}$, it may be both simpler and less ambiguous to use a method that does not involve density to calculate T_e.

To make the single atom calculations useful for estimating nebular temperatures, we need to fit a function to the data, which allows us to interpolate to observed values. In previous approaches to measuring electron temperatures, simple polynomials have been used to fit the flux ratio versus temperature plots. These are only stable over the range of fitted data, and extrapolating outside this range may lead to unreliable results. For example, the models of Seaton (1975) were limited to electron temperatures between 5000 and 20,000 K.

To avoid any instabilities, we fit the data using a rational polynomial, the ratio of two simple polynomials. Rational polynomials are generally stable outside the fitted data range. See (Press et al. 2007, Section 3.4) for a discussion of the benefits of fitting with rational polynomials. With the appropriate choice of variables, accurate fits can be found using low-order polynomials. Our fits are of the form shown in Equation (3), the ratio of a second and a third order polynomial:

$$\log_{10}(T_e) = \frac{P_0 + P_1 x + P_2 x^2}{1.0 + Q_1 x + Q_2 x^2 + Q_3 x^3} \qquad (3)$$

where x is the log of the flux ratio, and $P_{0,1,2}$ and $Q_{1,2,3}$ are the fit coefficients. For fit stability, these coefficients need to be small numbers, e.g. ~ 10 or less. In some cases the fits can be simplified further. We use an implementation of the Levenberg–Marquardt method (Press et al. 2007, Section 15.5.2) to fit the curves. It is worth noting that fitting rational polynomials does not always find the best fit, a situation that can be apparent when the parameters become very large. The fit found under such circumstances is valid but not likely to be the global best fit. Some experimenting with the combination of numerator and denominator polynomial orders may be necessary to identify the fit with the smallest parameters.

To illustrate the stability of the rational polynomial, Figure 5 shows the fit (blue line) and the actual (computed) flux ratio (dots) versus electron temperature, for fitted data between 5000 and 32,000 K. Log values are used to simplify the fit. The outer data point was not used in the fit, and indicates that the rational polynomial method can generate a fit which can (within reason) be trusted to give reliable extrapolation outside the fitted range, provided (a) that other physical effects do not come into play at temperatures outside the fitted region, and (b) that the roots of the denominator polynomial lie outside the extrapolation range.

The line ratios in this work are fit between 5000 and 32,000 K. They were calculated with the Mappings *V* 5.1 photoionization modeling application in simple atomic data mode, using full collisional and radiative excitation/de-excitation, and collisional

cross-section data from Lennon & Burke (1994). The models involve full cascade from higher levels. If necessary these calculations can be extended to far higher temperatures, but for the conditions likely to be encountered in H II regions, 32,000 K exceeds observational requirements.

Using the collisional cross-section data for O^{++} from Lennon & Burke (1994), for the ratio of fluxes of the 4363 Å line and the 4959 + 5007 Å lines, the best fit is expressed as the ratio of a linear and a cubic equation,

$$\log_{10}(T_e) = \frac{3.5363 + 7.2939x}{1.0000 + 1.6298x - 0.1221x^2 - 0.0074x^3} \quad (4)$$

where

$$x = \log_{10}\left(\frac{f_{4363}}{f_{4959} + f_{5007}}\right)$$

and f_{nnnn} is the flux of the emission line at nnnn Å. Note that we use an inverted form of the flux ratio compared to Equation (2), to avoid enhancing the effects of noise on measurements of low flux values of [O III] 4363 Å, and computational instabilities arising from dividing by a small number. Wesson et al. (2016) showed that this form of the flux ratio also avoids problems with large normally distributed uncertainties, which can become skewed if the smaller flux is used as denominator.

6.1. Comparison with Other Methods

How does the rational polynomial fit method compare with earlier methods? In Table 2 we compare it with the PyNeb routine and the Aller/Osterbrock/Izotov iterative routine to analyze four spherical models with differing pressure, ionization parameter, metallicity, and dust depletion.[8]

For electron densities up to ~1000 cm^{-3}, the simple method compares favourably with the other two methods, but as expected, at higher densities, it is less precise. However, even at n_e ~10,000 cm^{-3}, the error introduced by ignoring the density dependence is less than 2%, likely to be considerably less than the observational measurement uncertainty.

Figure 2 and Table 1 demonstrate that the local temperature through the [O III] emission region in spherical models can vary considerably for low and high metallicities, so the differences between the analysis methods are likely to be significantly smaller than the actual variations through the model. This is likely to be the case in real H II regions.

The rational polynomial method does not require knowing a priori the electron density whereas the other two methods require an estimate of the electron density, usually derived from the [S II] doublet. As noted earlier, the sulphur lines in an H II region are not co-spatial with the oxygen lines, so there is an additional uncertainty. For some objects, the density will be near the low density limit, so the uncertainty will not matter, but for extreme star-forming regions in high redshift H II regions, this uncertainty may be important.

[8] In the table "Pk6" means $\log(P/k) = 6$ where P is the pressure and k the Boltzmann constant, "Q7.5" means $\log(Q) = 7.5$ where Q is the ionization parameter, Z0.2 means $Z = 0.2$ solar where Z is the metallicity relative to solar, and "D-0.5" means the logarithmic dust depletion of Fe = −0.5, as discussed in Dopita et al. (2016, 2018).

Table 2
T_e Values Calculated Using Different Methods, Spherical Models

	PyNeb	Izotov06	This work
Model: Pk6.0 Q7.5 Z0.2 D-0.5 Average T_e (K) = 12160 S II mean n_e (cm^{-3}) = 37.9	12162	12132	12166
Model: Pk6.0 Q7.5 Z0.5 D-1.00 Average T_e (K) = 9700 S II mean n_e (cm^{-3}) = 45.9	9703	9704	9708
Model: Pk6.0 Q7.5 Z1.0 D-1.5 Average T_e (K) = 7999 S II mean n_e (cm^{-3}) = 56.1	8008	8024	8010
Model: Pk7.5 Q8.0 Z0.5 D-1.0 Average T_e (K) = 9987 S II mean n_e (cm^{-3}) = 1546	10026	10009	10030

Table 3
Intensities of the [O III] Lines Relative to λλ4363 for T_e = 12500 K, n_e = 10 cm^{-3}

Line(Å)	1660	1666	2321	2332	4363	4959	5007
Relative Intensity	0.43	1.25	0.25	0.78E-3	1.0	27.3	81.4

6.2. Using the UV lines of O^{++}

When the [O III] UV lines are available for ground-based observation, for example in high redshift objects, there are additional opportunities for estimating electron temperatures. Some of these lines are easier to observe than others. Table 3 shows the intensities of the UV [O III] lines relative to the 4363 Å line, for typical H II regions, providing a guide to how useful such lines are in measuring temperatures.

With present instrumentation and high redshift objects, only the 1666 Å and 4363 Å lines are likely to be observable with reasonable signal-to-noise and useful for temperature estimation, but with 20 meter class telescopes, other UV lines, in particular the 1660 and 2321 Å lines, may become useable, at least for unresolved near-point source objects. The emission line at 2321 Å arises from the same $^1S_0$ level as the 4363 Å line, and thus provides both a comparison, and an alternative when the 4363 Å line is not available. However, extinction correction is more difficult, due to the wavelength separation from the 4959 and 5007 Å lines.

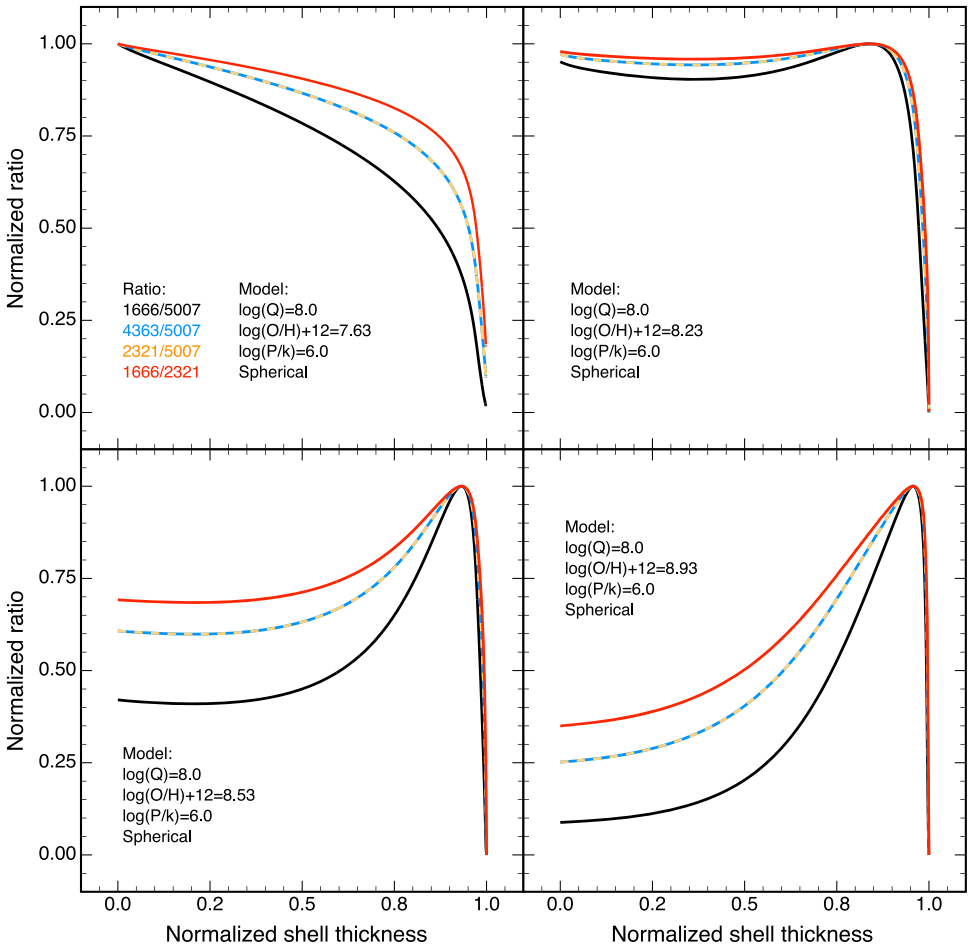

Figure 6. Showing the regions of greatest sensitivity of the [O III] line ratios for a spherical model H II region for a range of metallicities. Plane parallel models with the same parameters are closely similar. The curves are also similar for a range of values of log(Q) and log(P/k), at each metallicity. The normalized curves for 4363/5007 and 2321/5007 are virtually identical, as they arise from the same upper energy level
(A color version of this figure is available in the online journal.)

Table 4
Fit Parameters for [O III] Line Flux Ratios ($n_e = 100$ cm^{-3}), Using Collision Strengths from Lennon & Burke (1994)

Ratio	P_0	P_1	P_2	Q_1	Q_2	Q_3	rms fit error
1666/5007	5.3644	−10.7798	0.9348	−2.6064	0.3359	0.0000	2.41E-05
1666/2321	3.8379	−3.0804	0.4088	−0.8747	0.1456	0.0000	4.26E-05
1660 + 1666/5007	5.0485	−8.2350	0.6987	−2.0120	0.2510	0.0000	2.41E-05
1660 + 1666/2321	3.8040	−2.8589	0.3670	−0.8185	0.1307	0.0000	4.26E-05
2321/5007	4.0093	4.1823	0.0000	0.8653	−0.0760	−0.0043	3.15E-05
4363/5007	3.3027	9.1917	0.0000	2.092	−0.1503	−0.0093	3.15E-05
4363/5007 + 4959	3.5363	7.2939	0.0000	1.6298	−0.1221	−0.0074	3.15E-05

The 1666 Å line was used by Villar-Martín et al. (2004) to estimate the electron temperature in a redshift 3.36 galaxy, illustrating the increasing importance of UV emission lines in measuring physical conditions in high redshift nebulae. See also the discussion of high redshift pressure and density diagnostics in Kewley et al. (2019a).

Table 4 gives the values of the fit parameters for different flux ratios. The relative fit errors are all $<10^{-4}$ over the fitted range ($5000 < T_e < 32{,}000$ K).

In practice, this effect of ignoring the density sensitivity of the temperature diagnostic lines is small for electron densities $<5{,}000$ cm^{-3}. The variation with density is far less than the

Table 5
Temperatures Derived from Spherical Model Line Ratios Using the Parameters in Table 4 for Different Metallicities, $\log(Q) = 8.0$, and $\log(P/k) = 6.0$

Ratio	1666/5007	2321/5007	4363/5007	1666/2321
log(O/H)+12	T_e			
7.63	15702	15666	15667	15748
8.23	12188	12185	12185	12191
8.53	9448	9429	9429	9476
8.93	6212	6146	6146	6299

Note. This shows the intrinsic variation between different line ratios for a model H II region, and is indicative of the spread in measurements for a real nebula when using these line ratio calculations. The differences are principally due the radial sensitivities of the emission line ratios (see Figure 6). The values for the line ratio (1660+1666)/5007 are the same as for 1666/5007.

effects of observational uncertainties, making the use of the parametric fits very simple.

7. Line Flux Ratio Variation Through a Model Nebula

Figure 6 shows the radial variation of different line pair flux ratios in a spherical model H II regions at four metallicities. The curves show the variation in the sensitivity of the line ratios as temperature diagnostics to different regions in the nebula, and their variation with metallicity. This gives some indication of how the line ratios might respond to real H II regions. The models are calculated for $\log(O/H) = 7.63$, 8.23, 8.53, and 8.93, corresponding to 0.08, 0.32, 0.65, and 1.6 Solar for the standard values for bulk solar abundances from Asplund et al. (2009), an ionization parameter $\log(Q) = 8.0$, corresponding to a highly excited inner zone, at a pressure $\log(P/k) = 6.0$ (where P is the pressure and k is the Boltzmann constant). The curves are similar for lower values of $\log(Q)$ and $\log(P/k)$, and for plane parallel models, at each metallicity. The normalized curves for 4363/5007 and 2321/5007 are virtually identical, as they arise from the same upper energy level. The flux ratio of the 1666 and 2321 Å lines, for this model geometry, give the most uniform coverage of the nebula.

For the models in Figure 6, Table 5 shows the electron temperatures derived using the four line ratios for the integrated fluxes from the models. This shows the intrinsic variation between different line ratios for a model H II region, and is indicative of the spread in measurements for a real nebula when using these line ratio calculations. The differences arise from the radial sensitivities of the emission line ratios.

8. Observations of High Redshift Objects

As examples to use for estimating T_e in high redshift objects, we draw on observational data from Kojima et al. (2017),

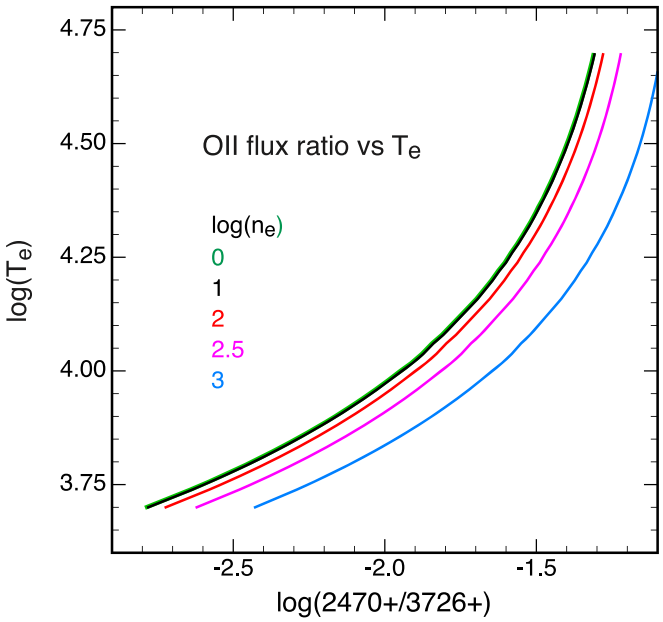

Figure 7. Flux ratio O II$_{(2470.2+2470.3)}$/O II$_{(3726+3729)}$ calculated as a function of temperature, using single atom models at fixed densities.
(A color version of this figure is available in the online journal.)

Christensen et al. (2012), Erb et al. (2010), Yuan & Kewley (2009), Bayliss et al. (2014), James et al. (2014), Steidel et al. (2016), and Villar-Martín et al. (2004). Table 6 is a compendium of published high redshift emission line data from these sources for the 1660, 1666, 4363 and 5007 Å lines of [O III].

Table 7 compares the electron temperature values from the published sources, and derived using the line ratio parameters from Table 4. The values in most cases are close, with the exception of the values involving the 1660 and 1666 Å fluxes for A1689 31.1. This discrepancy probably originates from uncertainties in the dust extinction and the de-reddening calculation, an intrinsic problem when using UV line fluxes. Another possible discrepancy source is enhanced flux from the 5S2 level due to the effect of high pressures.

9. [O_{II}] Lines as Electron Temperature Diagnostics

The [O II] emission lines at 3726 and 3729 Å are normally used as density diagnostics, but below electron densities $\sim 20\ \mathrm{cm}^{-3}$, the ratio of the line fluxes is not sensitive to density (Kewley et al. 2019a). This case is often referred to as the "low density limit." At these densities, in combination with the close doublet at 2470 Å, the 3726 and 3728 Å lines can provide a useful electron temperature diagnostic, with the benefit that the density and temperature species are the same, and therefore co-spatial. Calculated in the same manner as above, using

Table 6
Published Flux Observations for [O III] Emission Lines, Reddening-corrected, Relative to H_β

Source	Object	O III 1660	±	O III 1666	±	O III 4363	±	O III 4959	±	O III 5007	±
1	COSMOS 12805	0.049	0.012	0.075	0.015	⋯	⋯	1.890	0.420	6.460	0.290
2	A1689 31.1	0.440	0.100	1.000	0.140	0.171	0.061	1.429	0.364	4.722	0.608
2	SMACS J0304	0.042	0.010	0.068	0.011	⋯	⋯	1.313	0.006	4.582	0.014
2	SMACS J2031	0.089	0.021	0.269	0.027	⋯	⋯	1.638	0.078	5.421	0.197
3	Q2343 BX418	0.115	0.036	0.154	0.044	⋯	⋯	2.077	0.318	6.423	0.733
4	A 1689	⋯	⋯	⋯	⋯	0.270	0.100	1.980	0.300	6.450	0.300
5	SGAS J105039	0.056	0.031	0.169	0.089	< 0.206	⋯	2.375	0.825	7.938	3.038
6	Cassowary 20	0.110	0.110	0.260	0.130	0.050	0.030	1.650	0.100	4.880	0.280
7	30 stack	0.020	0.006	0.056	0.007	<0.06	⋯	1.420	0.020	4.250	0.020
8	Lynx arc	⋯	⋯	0.56[a]	0.04	⋯	⋯	⋯	⋯	7.50	0.3

Notes. Sources: 1: Kojima et al. (2017), 2: Christensen et al. (2012), 3: Erb et al. (2010), 4: Yuan & Kewley (2009), 5: Bayliss et al. (2014), 6: James et al. (2014), 7: Steidel et al. (2016) 8: Villar-Martín et al. (2004)
[a] 1660 and 1666 Å lines combined.

Table 7
Comparison of Electron Temperatures Published and Calculated using the Formulae

Source	Object	*Te* (Pubished)	Error	$Te\left(\frac{1660+66}{5007}\right)$	Error	$Te\left(\frac{1666}{5007}\right)$	Error	$Te\left(\frac{4363}{5007}\right)$	Error
1	COSMOS 12805	12900	$^{+8700}_{-900}$	12312	$^{+723}_{-682}$	11781	$^{+582}_{-614}$	⋯	⋯
2	A1689 31.1	21600[a]	$^{+3000}_{-3000}$	32073	$^{+4951}_{-6927}$	30789	$^{+5702}_{-4162}$	21120	$^{+7718}_{-5576}$
2	SMACS J0304	12900	$^{+90}_{-900}$	12937	$^{+602}_{-546}$	12409	$^{+428}_{-466}$	⋯	⋯
2	SMACS J2031	16100	$^{+300}_{-300}$	16847	$^{+865}_{-873}$	16888	$^{+708}_{-692}$	⋯	⋯
3	Q2343 BX418	15000	$^{+5000}_{-700}$	14821	$^{+1596}_{-1659}$	13861	$^{+1395}_{-1356}$	⋯	⋯
4	A 1689	23557	⋯	⋯	⋯	⋯	⋯	23316	$^{+8359}_{-5121}$
5	SGAS J105039	<14000	⋯	13446	$^{+2739}_{-3734}$	13470	$^{+3727}_{-2719}$	<17416	⋯
6	Cassowary 20	17000	$^{+3300}_{-3300}$	17582	$^{+4501}_{-3815}$	17260	$^{+2926}_{-3228}$	11696	$^{+4863}_{-621}$
7	30 stack	12250	$^{+600}_{-600}$	12092	$^{+479}_{-437}$	12096	$^{+323}_{-344}$	<13188	⋯
8	Lynx arc	17300	$^{+500}_{-700}$	17497	$^{+601}_{-627}$	⋯	⋯	⋯	⋯

Notes. Sources as per Table 6.
[a] Using 4363/5007 ratio.

Mappings *V* 5.1, Figure 7 shows how the flux ratio (2470.2 + 2470.3)/(3726 + 3729) varies as a function of electron temperature and density. If both the 2470 Å and 37269 Å pairs are observed, it is possible to use them to estimate the electron temperature. As before, the plot for $n_e = 10\,\mathrm{cm}^{-3}$ is well fit by a simple rational polynomial:

$$\log_{10}(T_e) = \frac{3.6289 + 4.4643x + 0.1893x^2}{1.000 + 1.0718x} \quad (5)$$

where

$$x = \log_{10}\left(\frac{f_{2470.2} + f_{2470.3}}{f_{3726} + f_{3729}}\right)$$

How well the [O II] and [O III] electron temperatures agree depends on the structure of the nebula. The [O II] emissions reflect electron temperatures in the outer nebular regions and the [O III] emissions the inner regions. An isothermal nebula will give the same results as [O III] provided the [O II] diagnostic is valid (i.e., low density). Table 8 shows the [O II] flux ratios for the 3726, 3729 Å lines, maximum model electron densities, [O II] and [O III] electron temperatures for plane-parallel models with $\log(Q) = 7.5$ and $\log(P/k) = 5.0$. The [O II] electron temperatures were calculated using Equation (5) and the [O III] electron temperatures using Equation (4). The "3729/6" column gives the flux ratio of the 3729 and 3726 Å [O II] lines, an indicator of when the ratio changes from a temperature to a density diagnostic, i.e.,

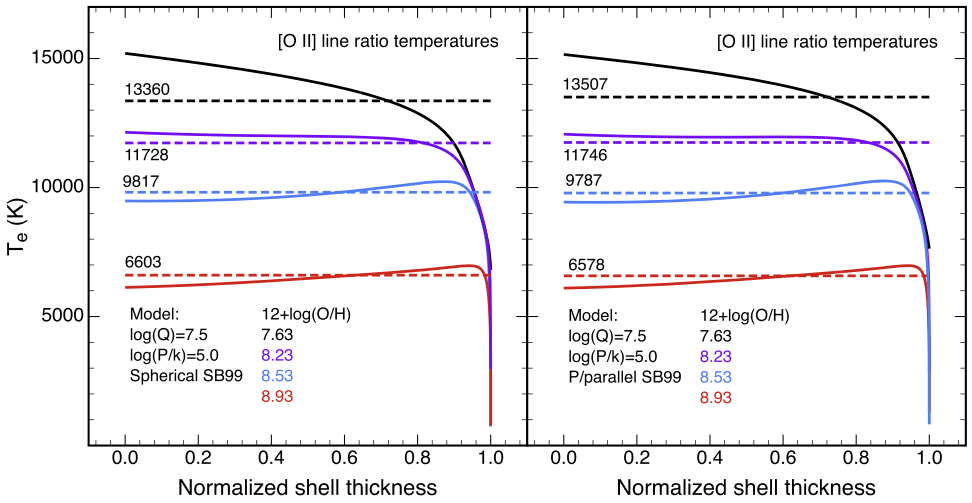

Figure 8. Electron temperature vs. normalized shell thickness of spherical and plane parallel models at different metallicities, for $\log(Q) = 7.5$ and $\log(P/k) = 5.0$. The dashed lines show the integrated flux temperatures using the [O II] doublets ratio using Equation (5).
(A color version of this figure is available in the online journal.)

Table 8
O II Flux Ratios, Electron Densities, Temperatures and O III Temperatures, Plane-parallel Model

log (Q)	log (P/k)	log(O/H)+12	3729/6	maxn_e	T_e O II (K)	T_e O III (K)	δT_e
7.5	5.0	7.63	1.454	4.1	13507	14434	**927**
		8.23	1.452	4.3	11746	11969	223
		8.53	1.449	5.3	9787	9572	−215
		8.93	1.440	8.2	6578	6299	−279
7.5	5.5	7.63	1.440	12.8	13594	14436	**842**
		8.23	1.436	13.5	11830	11978	148
		8.53	1.427	16.7	9878	9598	−280
		8.93	1.401	25.4	6768	6417	−351
8.0	5.5	7.63	1.441	12.8	14420	15826	**1406**
		8.23	1.436	13.5	12134	12113	−21
		8.53	1.426	17.9	9961	9309	−652
		8.93	1.394	30.0	6773	3599	**−3174**
8.0	6.0	7.63	1.403	40.4	14713	15830	**1117**
		8.23	1.386	42.5	12408	12141	−267
		8.53	1.360	56.3	10223	9371	**−852**
		8.93	1.280	90.6	7086	6111	**−975**
8.5	6.0	7.63	1.401	42.3	14576	16433	**1857**
		8.23	1.383	45.5	12838	12369	−469
		8.53	1.349	64.5	10604	9366	**−1238**
		8.93	1.231	121.6	7417	6033	**−1384**

Note. The temperatures are in reasonable agreement for $\log(P/k) \leqslant 5.5$ and $\log(O/H)+12 \geqslant 8.23$. Bold face numbers in the δT_e column indicate large discrepancies between the two temperatures.

below ∼1.42. The "max n_e" column shows the maximum value of the electron density calculated in each model. Where these values are <20, the ratio is a temperature diagnostic in the region where the [O II] lines are emitted.

In Table 8, the column "δT_e" shows the difference between [O III] and [O II] temperatures. Bold face numbers show large discrepancies. Note that these tend to occur for high or low metallicity. Substantially different [O III] and [O II] temperatures are thus an abundance indicator, with a positive discrepancy[9] indicating low abundance, and a negative discrepancy indicating high abundance.

Figure 8 shows the electron temperature versus normalized shell thickness for similar spherical and plane parallel models at different metallicities, for $\log(Q) = 7.5$ and $\log(P/k) = 5.0$. The dashed lines show the integrated flux temperatures using the [O II] doublets ratio in Equation (5). The slight differences are due to the difference in geometries of the models, and suggest that the behavior does not vary dramatically with small changes in geometry.

Figure 9 (left panel) shows the radial dependence of the flux ratio $[\mathrm{O\,II}]_{(2470.2+2470.3)}/[\mathrm{O\,II}]_{(3726+3729)}$ at a metallicity $\log(O/H) + 12 = 8.23$ for two values $\log(Q)$ and $\log(P/k)$. The right panel shows the radial distribution of the [O II] 3729 Å emission line and the considerable difference between higher and lower excitation nebulae.

10. Other Ions

While it is outside the scope of this paper, it is worth noting that other ionic species observed in H II regions can be used to measure electron temperatures, such as O, N^+, S^{++} and Ne^{++}. All of these have at least two approximately evenly spaced energy levels about the ground state(s), with energy differences $\sim kT_e$. The advantage of using these lines is that their emission lines arise in part in different zones of the ionized region, and

[9] i.e., $T_e([\mathrm{O\,III}]) > T_e([\mathrm{O\,II}])$.

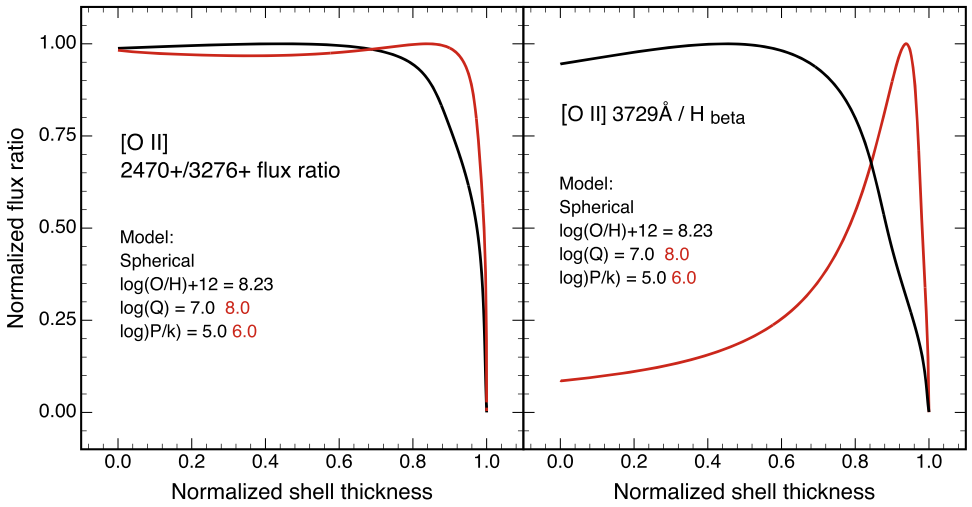

Figure 9. Left panel: variation of the flux ratio of the [O II 2470] and 3726 + 9 Å emission lines through a spherical H II region model with metallicity log(O/H) + 12 = 8.23, for different log(Q) and log(P/k). Right panel: radial distribution of the [O II]] 3729 Å emission line and the considerable difference between higher and lower excitation nebulae
(A color version of this figure is available in the online journal.)

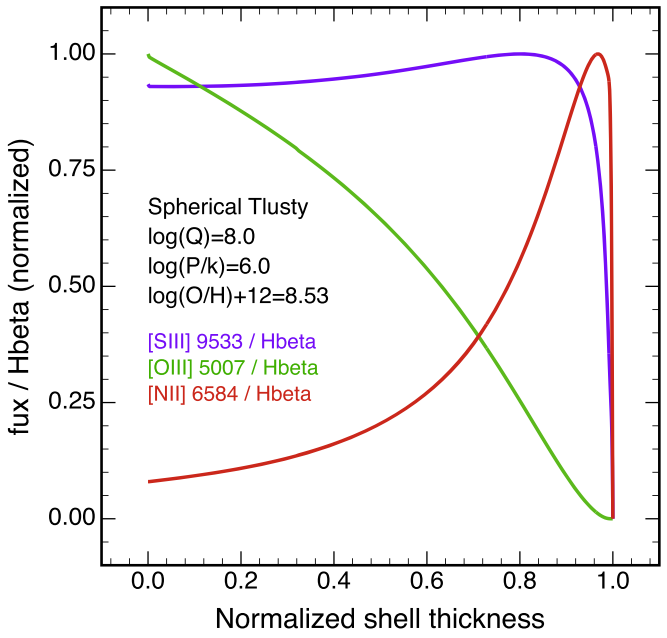

Figure 10. Radial distribution of key ion emission lines, spherical H II region model with metallicity log(O/H)+12 = 8.53, log(Q) = 8.0 and log(P/k) = 6.0, illustrating where they are most sensitive to the electron temperature.
(A color version of this figure is available in the online journal.)

therefore provide a measure of temperatures in zones not well represented by the [O III] lines, allowing a more complete picture of the temperature distribution throughout the nebula. The requirement is that a species have the necessary observable emission lines and that the electron density be well below the critical density for the species. Figure 10 shows the emission line fluxes of the readily observable optical lines [O III] 5007 Å, [S III] 9533 Å, and [N II] 6584 Å for a simple single central star spherical model (Tlusty O-star stellar atmosphere, $T = 40\,k$K, log(g) = 4.0, metallicity M03 Lanz & Hubeny 2003).

11. Conclusion

When will electron temperature diagnostics give reasonable results in an H II region? We cannot be sure. Where the structure of an H II region is resolved, such as in nearby galaxies, and when it is simple, e.g., approximately spherical or plane parallel, and approximately at constant pressure, the models used here suggest that for intermediate metallicities, $0.2 < z < 1$ solar, the standard oxygen line diagnostics can give quite good estimates of T_e. For distant unresolved H II regions, which are generally large, complex structures, it is likely that electron temperature estimates will at best be a means of ranking nebulae in terms of metallicity, and identifying trends in metallicity.

For electron densities below ~5000 cm^{-3}, there is little to be gained by taking density into account in calculating the electron temperature. The uncertainties in what observations actually measure, i.e., the comparison of observations to single atom isothermal models, the use of densities derived from ions not co-spatial with [O III] emissions, and the bias of observed fluxes in unresolved emission regions to zones of high

pressure, mean that precision fitting of the models may give slightly different results (typically ∼100K) than a single density fit, but the differences convey little useful physical information. We can only derive an approximate value for the electron temperature. Combined with the S/N of the observations, significant for distant high redshift objects, we can only derive an approximation to the true physics of what we observe. A "characteristic" electron temperature is what we should aim for.

The formulae presented here are simple to use, but they are a compromise, derived for an electron density of 100 cm^{-3}. The parameters change with increasing density, so no single set is precise for all densities. Other inputs (e.g., from Table 9) can be used to generate rational polynomial fits tailored to a specific density. However, the parameters presented in Table 4 are sufficiently accurate for the purpose of deriving estimates of electron temperatures for electron densities $<5000\,cm^{-3}$.

Observations of UV lines of [O II] and [O III] are now possible for H II regions and other bright emission regions in high redshift objects. Such observations will become standard results with the coming generation of large telescopes. The formulae presented here can be used to estimate electron temperatures in these objects, and the different line pairs provide useful comparisons. Comparing the results using the formulae to published high redshift observations shows the differences are mostly small and within observational uncertainties.

Finally, it is clear that using a single atom model to estimate electron temperatures in nebulae is at best an approximation, an *atomic equivalent temperature*, as nebulae are not isothermal. The best approach to modeling nebulae involves using applications such as Cloudy or Mappings, and fitting the model line fluxes of different ionic species simultaneously to the observed data.

This research was conducted under the auspices of the Australian Research Council Centre of Excellence for All Sky Astrophysics in 3 Dimensions (ASTRO 3D), through project number CE170100013. The authors would like to acknowledge the late Professor Mike Dopita who has been a guide and inspiration to us, and who provided comments on an early version of this paper.

Appendix
Flux Ratios as a Function of Electron Density and Electron Temperature

Table 9
[O III] Line Flux Ratios as a Function of Temperature and Density

	$n_e = 1$				$n_e = 10$				$n_e = 100$			
T_e	1666/2321	1666/5007	2321/5007	4363/5007	1666/2321	1666/5007	2321/5007	4363/5007	1666/2321	1666/5007	2321/5007	4363/5007
2000	1.437-04	4.258-13	2.962-09	1.178-08	1.436-04	4.253-13	2.963-09	1.178-08	1.426-04	4.226-13	2.964-09	1.178-08
3000	9.074-03	6.605-09	7.279-07	2.893-06	9.066-03	6.599-09	7.279-07	2.893-06	9.014-03	6.562-09	7.280-07	2.894-06
4000	7.280-02	8.296-07	1.140-05	4.530-05	7.274-02	8.290-07	1.140-05	4.530-05	7.236-02	8.250-07	1.140-05	4.532-05
5000	2.548-01	1.509-05	5.921-05	2.354-04	2.547-01	1.508-05	5.922-05	2.354-04	2.534-01	1.502-05	5.927-05	2.356-04
6000	5.876-01	1.042-04	1.773-04	7.049-04	5.872-01	1.042-04	1.774-04	7.050-04	5.845-01	1.038-04	1.776-04	7.059-04
7000	1.065 + 00	4.135-04	3.882-04	1.543-03	1.065 + 00	4.134-04	3.883-04	1.543-03	1.060 + 00	4.122-04	3.888-04	1.545-03
8000	1.660 + 00	1.161-03	6.991-04	2.779-03	1.659 + 00	1.160-03	6.992-04	2.779-03	1.654 + 00	1.158-03	7.000-04	2.783-03
9000	2.338 + 00	2.584-03	1.105-03	4.394-03	2.337 + 00	2.584-03	1.106-03	4.394-03	2.332 + 00	2.580-03	1.107-03	4.399-03
10000	3.068 + 00	4.895-03	1.596-03	6.342-03	3.067 + 00	4.894-03	1.596-03	6.343-03	3.062 + 00	4.889-03	1.597-03	6.347-03
11000	3.823 + 00	8.239-03	2.155-03	8.566-03	3.823 + 00	8.238-03	2.155-03	8.566-03	3.819 + 00	8.234-03	2.156-03	8.570-03
12000	4.585 + 00	1.269-02	2.769-03	1.101-02	4.585 + 00	1.269-02	2.769-03	1.101-02	4.583 + 00	1.269-02	2.769-03	1.101-02
13000	5.339 + 00	1.828-02	3.423-03	1.361-02	5.339 + 00	1.828-02	3.423-03	1.361-02	5.339 + 00	1.828-02	3.424-03	1.361-02
14000	6.076 + 00	2.494-02	4.106-03	1.632-02	6.076 + 00	2.495-02	4.106-03	1.632-02	6.078 + 00	2.496-02	4.106-03	1.632-02
15000	6.788 + 00	3.263-02	4.806-03	1.910-02	6.789 + 00	3.263-02	4.806-03	1.910-02	6.792 + 00	3.265-02	4.807-03	1.911-02
16000	7.473 + 00	4.122-02	5.516-03	2.193-02	7.474 + 00	4.123-02	5.516-03	2.193-02	7.478 + 00	4.126-02	5.517-03	2.193-02
17000	8.128 + 00	5.062-02	6.228-03	2.476-02	8.129 + 00	5.063-02	6.228-03	2.476-02	8.134 + 00	5.067-02	6.230-03	2.476-02
18000	8.752 + 00	6.072-02	6.937-03	2.758-02	8.753 + 00	6.073-02	6.938-03	2.758-02	8.758 + 00	6.078-02	6.940-03	2.758-02
19000	9.345 + 00	7.140-02	7.640-03	3.037-02	9.346 + 00	7.141-02	7.640-03	3.037-02	9.351 + 00	7.147-02	7.643-03	3.038-02
20000	9.908 + 00	8.255-02	8.332-03	3.312-02	9.909 + 00	8.256-02	8.332-03	3.312-02	9.914 + 00	8.264-02	8.336-03	3.313-02
22000	1.095 + 01	1.059-01	9.677-03	3.846-02	1.095 + 01	1.059-01	9.678-03	3.847-02	1.095 + 01	1.060-01	9.683-03	3.849-02
24000	1.187 + 01	1.301-01	1.096-02	4.356-02	1.188 + 01	1.302-01	1.096-02	4.357-02	1.188 + 01	1.303-01	1.097-02	4.360-02
26000	1.271 + 01	1.547-01	1.218-02	4.840-02	1.271 + 01	1.547-01	1.218-02	4.840-02	1.271 + 01	1.548-01	1.219-02	4.844-02
28000	1.345 + 01	1.792-01	1.332-02	5.295-02	1.345 + 01	1.792-01	1.332-02	5.296-02	1.345 + 01	1.793-01	1.333-02	5.300-02
30000	1.412 + 01	2.033-01	1.440-02	5.724-02	1.411 + 01	2.033-01	1.440-02	5.725-02	1.411 + 01	2.034-01	1.441-02	5.729-02
32000	1.471 + 01	2.268-01	1.541-02	6.127-02	1.471 + 01	2.268-01	1.541-02	6.127-02	1.471 + 01	2.269-01	1.543-02	6.132-02
34000	1.525 + 01	2.495-01	1.636-02	6.505-02	1.525 + 01	2.495-01	1.637-02	6.505-02	1.524 + 01	2.496-01	1.638-02	6.510-02
36000	1.573 + 01	2.714-01	1.726-02	6.860-02	1.573 + 01	2.715-01	1.726-02	6.860-02	1.572 + 01	2.715-01	1.727-02	6.865-02
38000	1.616 + 01	2.925-01	1.810-02	7.193-02	1.616 + 01	2.925-01	1.810-02	7.193-02	1.616 + 01	2.925-01	1.811-02	7.198-02

Table 9
(Continued)

	$n_e = 1$				$n_e = 10$				$n_e = 100$			
T_e	1666/2321	1666/5007	2321/5007	4363/5007	1666/2321	1666/5007	2321/5007	4363/5007	1666/2321	1666/5007	2321/5007	4363/5007
40000	1.655 + 01	3.126-01	1.888-02	7.506-02	1.655 + 01	3.126-01	1.888-02	7.506-02	1.655 + 01	3.126-01	1.889-02	7.510-02
42000	1.691 + 01	3.318-01	1.962-02	7.800-02	1.691 + 01	3.318-01	1.962-02	7.800-02	1.690 + 01	3.318-01	1.963-02	7.804-02
44000	1.723 + 01	3.501-01	2.032-02	8.077-02	1.723 + 01	3.501-01	2.032-02	8.077-02	1.722 + 01	3.501-01	2.033-02	8.080-02
46000	1.752 + 01	3.675-01	2.097-02	8.337-02	1.752 + 01	3.675-01	2.098-02	8.337-02	1.751 + 01	3.675-01	2.098-02	8.340-02
48000	1.779 + 01	3.840-01	2.159-02	8.582-02	1.779 + 01	3.840-01	2.159-02	8.583-02	1.778 + 01	3.840-01	2.160-02	8.585-02
50000	1.803 + 01	3.997-01	2.217-02	8.814-02	1.803 + 01	3.997-01	2.217-02	8.814-02	1.802 + 01	3.997-01	2.218-02	8.816-02

	$n_e = 1000$				$n_e = 10000$			
T_e	1666/2321	1666/5007	2321/5007	4363/5007	1666/2321	1666/5007	2321/5007	4363/5007
2000	1.407-04	4.197-13	2.983-09	1.186-08	1.349-04	4.303-13	3.191-09	1.268-08
3000	8.899-03	6.515-09	7.320-07	2.910-06	8.577-03	6.643-09	7.744-07	3.078-06
4000	7.144-02	8.190-07	1.146-05	4.557-05	6.903-02	8.326-07	1.206-05	4.795-05
5000	2.502-01	1.492-05	5.965-05	2.371-04	2.421-01	1.515-05	6.257-05	2.487-04
6000	5.773-01	1.032-04	1.789-04	7.109-04	5.592-01	1.047-04	1.873-04	7.444-04
7000	1.048 + 00	4.105-04	3.916-04	1.557-03	1.017 + 00	4.162-04	4.093-04	1.627-03
8000	1.638 + 00	1.154-03	7.047-04	2.801-03	1.591 + 00	1.170-03	7.352-04	2.922-03
9000	2.314 + 00	2.575-03	1.113-03	4.424-03	2.251 + 00	2.609-03	1.159-03	4.606-03
10000	3.044 + 00	4.884-03	1.604-03	6.377-03	2.967 + 00	4.946-03	1.667-03	6.627-03
11000	3.804 + 00	8.232-03	2.164-03	8.603-03	3.712 + 00	8.333-03	2.245-03	8.923-03
12000	4.571 + 00	1.270-02	2.778-03	1.104-02	4.467 + 00	1.285-02	2.877-03	1.144-02
13000	5.331 + 00	1.830-02	3.433-03	1.364-02	5.216 + 00	1.851-02	3.549-03	1.411-02
14000	6.074 + 00	2.500-02	4.115-03	1.636-02	5.949 + 00	2.528-02	4.249-03	1.689-02
15000	6.793 + 00	3.272-02	4.817-03	1.915-02	6.659 + 00	3.308-02	4.968-03	1.975-02
16000	7.482 + 00	4.136-02	5.528-03	2.197-02	7.341 + 00	4.181-02	5.696-03	2.264-02
17000	8.139 + 00	5.081-02	6.243-03	2.481-02	7.991 + 00	5.136-02	6.427-03	2.555-02
18000	8.764 + 00	6.096-02	6.955-03	2.765-02	8.610 + 00	6.161-02	7.156-03	2.844-02
19000	9.357 + 00	7.169-02	7.662-03	3.045-02	9.197 + 00	7.245-02	7.878-03	3.131-02
20000	9.918 + 00	8.290-02	8.358-03	3.322-02	9.754 + 00	8.377-02	8.589-03	3.414-02
22000	1.095 + 01	1.064-01	9.712-03	3.861-02	1.078 + 01	1.075-01	9.971-03	3.963-02
24000	1.187 + 01	1.307-01	1.100-02	4.374-02	1.169 + 01	1.320-01	1.129-02	4.488-02
26000	1.270 + 01	1.553-01	1.223-02	4.861-02	1.251 + 01	1.568-01	1.254-02	4.984-02
28000	1.343 + 01	1.798-01	1.338-02	5.320-02	1.324 + 01	1.816-01	1.371-02	5.451-02
30000	1.409 + 01	2.039-01	1.447-02	5.751-02	1.390 + 01	2.059-01	1.482-02	5.889-02
32000	1.468 + 01	2.274-01	1.549-02	6.155-02	1.448 + 01	2.296-01	1.585-02	6.300-02
34000	1.521 + 01	2.501-01	1.644-02	6.535-02	1.501 + 01	2.525-01	1.682-02	6.684-02
36000	1.569 + 01	2.720-01	1.733-02	6.890-02	1.549 + 01	2.745-01	1.772-02	7.044-02
38000	1.612 + 01	2.930-01	1.817-02	7.222-02	1.592 + 01	2.956-01	1.857-02	7.380-02
40000	1.651 + 01	3.130-01	1.895-02	7.534-02	1.631 + 01	3.157-01	1.936-02	7.694-02
42000	1.687 + 01	3.322-01	1.969-02	7.827-02	1.667 + 01	3.350-01	2.010-02	7.988-02
44000	1.719 + 01	3.504-01	2.038-02	8.102-02	1.699 + 01	3.532-01	2.079-02	8.264-02
46000	1.748 + 01	3.677-01	2.103-02	8.360-02	1.728 + 01	3.706-01	2.144-02	8.523-02
48000	1.775 + 01	3.842-01	2.164-02	8.603-02	1.755 + 01	3.871-01	2.205-02	8.766-02
50000	1.799 + 01	3.998-01	2.222-02	8.832-02	1.780 + 01	4.027-01	2.263-02	8.994-02

Note. In this table, the notation 2.345-01 means 2.345×10^{-1}.

ORCID iDs

David C. Nicholls https://orcid.org/0000-0003-0892-5203

References

Aller, L. H. 1984, Physics of Thermal Gaseous Nebulae, Vol. 112 (Dordrecht: D. Reidel Publishing Co.)
Asplund, M., Grevesse, N., Sauval, A. J., & Scott, P. 2009, ARA&A, 47, 481
Baskin, A., & Laor, A. 2005, MNRAS, 358, 1043
Bayliss, M. B., Rigby, J. R., Sharon, K., et al. 2014, ApJ, 790, 144
Binette, L., Matadamas, R., Hägele, G. F., et al. 2012, A&A, 547, A29
Bohm, D., & Aller, L. H. 1947, ApJ, 105, 131
Bowen, I. S. 1928, ApJ, 67, 1
Christensen, L., Laursen, P., Richard, J., et al. 2012, MNRAS, 427, 1973
Dopita, M. A., Seitenzahl, I. R., Sutherland, R. S., et al. 2016, ApJ, 826, 150
Dopita, M. A., Vogt, F. P. A., Sutherland, R. S., et al. 2018, ApJS, 237, 10
Erb, D. K., Pettini, M., Shapley, A. E., et al. 2010, ApJ, 719, 1168

Evans, C. J., Taylor, W. D., Hénault-Brunet, V., et al. 2011, A&A, 530, A108
Hebb, M. H., & Menzel, D. H. 1940, ApJ, 92, 408
Izotov, Y. I., Stasińska, G., Meynet, G., Guseva, N. G., & Thuan, T. X. 2006, A&A, 448, 955
James, B. L., Pettini, M., Christensen, L., et al. 2014, MNRAS, 440, 1794
Kaplan, S. A. 1966, Interstellar Gas Dynamics (2nd ed.; Oxford: Pergamon Press)
Kewley, L. J., Nicholls, D. C., Sutherland, R., et al. 2019a, ApJ, 880, 16
Kewley, L. J., Nicholls, D. C., & Sutherland, R. S. 2019b, ARA&A, 57, 511
Kojima, T., Ouchi, M., Nakajima, K., et al. 2017, PASJ, 69, 44
Lanz, T., & Hubeny, I. 2003, ApJS, 146, 417
Leitherer, C., Ekström, S., Meynet, G., et al. 2014, ApJS, 212, 14
Lennon, D. J., & Burke, V. M. 1994, A&AS, 103, 273
Livadiotis, G. 2018, EL, 122, 50001
Luridiana, V., Morisset, C., & Shaw, R. A. 2012, in IAU Symp. 283, Planetary Nebulae: An Eye to the Future, ed. A. Manchado, L. Stanghellini, & Schönberner (Vienna: International Astronomical Union), 422
Nagao, T., Murayama, T., & Taniguchi, Y. 2001, ApJ, 549, 155
Nicholls, D. C., Dopita, M. A., & Sutherland, R. S. 2012, ApJ, 752, 148
Osterbrock, D. E. 1989, Astrophysics of Gaseous Nebulae and Active Galactic Nuclei (Sausalito, CA: Univ. Science Books)
Osterbrock, D. E., & Ferland, G. J. 2006, Astrophysics of gaseous nebulae and active galactic nuclei (2nd ed.; Mill Valley, CA: Univ. Science Books)
Palay, E., Nahar, S. N., Pradhan, A. K., & Eissner, W. 2012, MNRAS, 423, L35
Press, W. H., Teukolsky, S. A., Vetterling, W. T., & Flannery, B. P. 2007, Numerical Recipes: The Art of Scientific Computing (3rd ed.; Cambridge: Cambridge Univ. Press)
Seaton, M. J. 1975, MNRAS, 170, 475
Spitzer, L. 1968, Diffuse Matter in Space (New York: Interscience Publication)
Stasińska, G. 2004, in Cosmochemistry. The melting Pot of the Elements, ed. C. Esteban et al. (Cambridge Univ. Press: Cambridge), 115
Steidel, C. C., Strom, A. L., Pettini, M., et al. 2016, ApJ, 826, 159
Storey, P. J., Sochi, T., & Badnell, N. R. 2014, MNRAS, 441, 3028
Sutherland, R. S. 2019, MAPPINGS: Astrophysical equilibrium and time-dependent photoinisation and steady supersonic shock spectral emission code, https://bitbucket.org/RalphSutherland/mappings/src/master/
Villar-Martín, M., Cerviño, M., & González Delgado, R. M. 2004, MNRAS, 355, 1132
Wesson, R., Stock, D. J., & Scicluna, P. 2012, MNRAS, 422, 3516
Wesson, R., Stock, D. J., & Scicluna, P. 2016, MNRAS, 459, 3475
Yuan, T.-T., & Kewley, L. J. 2009, ApJL, 699, L161